The Astrophysical Journal, 681:1017–1034, 2008 July 10

THE X-RAY PROPERTIES OF MODERATE-REDSHIFT GALAXY GROUPS SELECTED BY ASSOCIATION WITH GRAVITATIONAL LENSES

C. D. Fassnacht, D. D. Kocevski, M. W. Auger, L. M. Lubin, and J. L. Neureuther
Department of Physics, University of California, Davis, 1 Shields Avenue, Davis, CA 95616; fassnacht@physics.ucdavis.edu

T. E. Jeltema
UCO/Lick Observatories, 1156 High Street, Santa Cruz, CA 95064

J. S. Mulchaey
Observatories of the Carnegie Institute of Washington, 813 Santa Barbara Street, Pasadena, CA 91101

and

J. P. McKean
Max-Planck-Institut für Radioastronomie, Auf dem Hügel 69, D-53121 Bonn, Germany
Received 2007 November 13; accepted 2008 March 6

ABSTRACT

We present results from a systematic investigation of the X-ray properties of a sample of moderate-redshift ($0.3 < z < 0.6$) galaxy groups. These groups were selected not by traditional X-ray or optical search methods, but rather by an association, either physical or along the line of sight, with a strong gravitational lens. We calculate the properties of seven galaxy groups in the fields of six lens systems. Diffuse X-ray emission from the intragroup medium is detected in four of the groups. All of the detected groups have X-ray luminosities greater than $10^{42}\ h^{-2}$ ergs s^{-1} and lie on the L_X-σ_v relations defined by local groups and clusters. The upper limits for the nondetections are also consistent with the local L_X-σ_v relationships. Although the sample size is small and deeper optical and X-ray data are needed, these results suggest that lens-selected groups are similar to X-ray–selected samples and thus are more massive than the typical poor-group environments of local galaxies.

Subject headings: galaxies: clusters: general — gravitational lensing — X-rays: galaxies: clusters

1. INTRODUCTION

To have a full picture of galaxy evolution and structure formation in the universe, it is crucial to understand the properties of galaxy groups. Most galaxies in the local universe reside in galaxy groups (e.g., Turner & Gott 1976; Geller & Huchra 1983; Eke et al. 2004). In addition, groups are vitally important in driving changes in star formation rates and galaxy morphologies since $z \sim 1$, because the low velocity dispersions and high density of groups make them likely locations for interactions and mergers (e.g., Aarseth & Fall 1980; Barnes 1985; Merritt 1985). Furthermore, indications are that the dark matter distributions in groups represent a transition between the dark matter–dominated profiles seen on cluster scales and galaxy-sized halos that are strongly affected by baryon cooling (e.g., Oguri 2005). In this paper we examine the properties of moderate-redshift groups.

Groups in the local universe have been well studied (e.g., Zabludoff & Mulchaey 1998; Mulchaey & Zabludoff 1998; Osmond & Ponman 2004; Rasmussen et al. 2006). In a systematic survey of 60 groups in the Group Evolution Multiwavelength Study (GEMS), Osmond & Ponman (2004) find that groups in the local universe obey L_X-σ_v and L_X-T scaling relations similar to those for more massive clusters, although a more recent analysis (S. F. Helsdon & T. J. Ponman 2008, in preparation) finds a steepening in the L_X-T slope for these groups. There is also a large nonstatistical scatter of a factor of 30 in X-ray luminosity and a factor of 3–4 in X-ray temperature for this group sample. This scatter includes a class of spiral-rich groups with little or no emission, as well as some groups with high X-ray luminosities but low velocity dispersions. Possible explanations for these outliers include unrelaxed dynamical states, uncertain velocity dispersion measures from small numbers of redshifts (typically fewer than 10; see also Zabludoff & Mulchaey 1998), and point-source contamination of the X-ray flux (Helsdon et al. 2005). Osmond & Ponman (2004) also find a strong correlation between the detection of diffuse emission and the presence of a centrally located, dominant early-type galaxy, as well as an anticorrelation between spiral fraction and gas temperature.

Additional outliers from the canonical scaling relations are found by Rasmussen et al. (2006), who are studying a redshift-selected, statistically unbiased sample of galaxy groups at $z \approx 0.06$ with deep X-ray data. The first galaxy groups detected by this survey are X-ray faint ($\sim 5 \times 10^{40}\ h^{-2}$ ergs s^{-1}), are underluminous for their measured velocity dispersions, and do not host a dominant, central early-type galaxy, suggesting that they are collapsing for the first time. Optically selected groups such as these represent a different, perhaps more common, class of groups than those detected through their X-ray emission.

Detailed studies of groups at moderate to high redshifts have been limited because groups are difficult to find, given their modest galaxy overdensities and X-ray luminosities. On the optical side, the situation has been alleviated somewhat by large redshift surveys such as the Sloan Digital Sky Survey (SDSS; York et al. 2000), the Canadian Network for Observational Cosmology Field Galaxy Survey (CNOC2; Yee et al. 2000), and the DEEP2 survey (Davis et al. 2003), but many of the group candidates found in these surveys have only three or four members (e.g., Carlberg et al. 2001; Gerke et al. 2005) and may not represent physically bound structures. Furthermore, the intensive spectroscopic follow-up required to confirm each group candidate and characterize its properties has so far limited the size of well-studied group samples from these surveys (e.g., Wilman et al. 2005; Balogh et al. 2007; Fang et al. 2007).

Intermediate-redshift ($0.2 < z < 0.6$) groups selected on the basis of their X-ray emission are also being studied (Willis et al.

2005a, 2005b; Mulchaey et al. 1996; Jeltema et al. 2006, 2007). Results for these surveys suggest that these groups follow the low-redshift scaling relations between luminosity, temperature, and velocity dispersion. Many of these systems have high fractions of early-type galaxies, suggesting that this population was already in place by $z \sim 0.5$ (Mulchaey et al. 1996; Jeltema et al. 2007). However, there are clear indications of dynamical evolution, including many groups with brightest group galaxies that show multiple components, dominant early-type galaxies that are not centered on the diffuse emission, or no dominant early-type galaxies at all. While similar systems have been identified in low-redshift samples (see above), the luminosities and temperatures of the moderate-redshift examples are significantly higher, implying a group downsizing in which more massive groups are still in the process of collapsing and virializing at these redshifts. The effects of evolution appear to continue to higher redshifts for which studies of some optically selected groups suggest that they are substantially and systematically underluminous relative to their local counterparts for a given velocity dispersion (Fang et al. 2007). Note, however, that the velocity dispersions in Fang et al. (2007) are all based on a small number of measured redshifts (ranging from 3 to 6 redshifts per group), and thus they are highly uncertain and may be significantly overestimated.

Significant differences between the properties of X-ray–and optically selected groups have been noted at both low and intermediate redshift (e.g., Rasmussen et al. 2006; Fang et al. 2007; Rykoff et al. 2008), suggesting that each method is selecting a distinct class of groups. To avoid these biases, we are conducting a survey of moderate-redshift groups that have been selected via a nontraditional technique, namely, through their association with strong gravitational lenses. There is growing evidence that strong gravitational lenses, i.e., those forming multiple images of the background object, are typically located in groups of galaxies at intermediate redshift (e.g., Kundić et al. 1997a, 1997b; Tonry 1998; Momcheva et al. 2006; Fassnacht et al. 2006a; Auger et al. 2007, 2008). Thus, strong lenses can be used to identify and study the properties of distant groups, selected in a manner that is completely independent of alternative techniques such as deep X-ray integrations or color-magnitude diagrams. The lensing probability depends only on the projected mass distribution and does not depend on its kinematics or on the properties of the galaxy population or intragroup medium (IGM). Therefore, lens-selected groups provide an excellent sample to determine the properties of galaxies and hot baryons and to understand selection effects (e.g., mass concentration for lensing, IGM luminosity and temperature for X-ray selection, and the homogeneity of the galaxy population for red sequence selection) by contrasting different methods.

It is not unexpected that the lensing galaxies in strong lens systems should reside in overdense regions of the universe. Searches for gravitational lenses are biased toward high-density regions because (1) higher mass systems have a larger cross section for lensing and (2) most lensing galaxies are ellipticals, which are preferentially found in groups or clusters (e.g., Dressler 1980; Zabludoff & Mulchaey 1998). Theoretical studies have predicted that a significant number of lens systems should be associated with groups or clusters, albeit with a large spread of values (Keeton et al. 2000; Holder & Schechter 2003; Oguri et al. 2005). Unbiased photometric surveys of lens fields indicate that lenses lie along overdense lines of sight (Williams et al. 2006; C. D. Fassnacht et al. 2008, in preparation), and spectroscopic observations have confirmed several lens-group associations that can affect the lensing potential at the level of 5% or more (e.g., Kundić et al. 1997a, 1997b; Tonry 1998; Fassnacht & Lubin 2002; Momcheva et al. 2006; Fassnacht et al. 2006a; Auger et al. 2007, 2008).

In this paper, we present the results from multiobject spectroscopic and deep *Chandra* observations of seven groups detected through their association with gravitational lenses. We assume a cosmological model with $(\Omega_m, \Omega_\Lambda) = (0.3, 0.7)$. We use $h = H_0/100$ km s^{-1} Mpc^{-1} to represent the Hubble constant when we do not have to choose a value. When we do have to assign a value to the Hubble constant, we use $h = 0.7$.

2. THE SAMPLE

The systems analyzed for this paper are all strong lenses for which we have obtained new observations with *Chandra* or for which data are available in the *Chandra* archive. Furthermore, each system had to show evidence of an associated galaxy group, obtained through spectroscopic surveys of the galaxies surrounding the main lens system. The targeted systems are described briefly below.

2.1. *CLASS B0712+472*

This four-image lens system (hereafter B0712) was discovered by Jackson et al. (1998) as part of the Cosmic Lens All-Sky Survey (CLASS; Myers et al. 2003; Browne et al. 2003). The lensing galaxy is at a redshift of $z_{\rm lens} = 0.406$ (Fassnacht & Cohen 1998), while the lensed source is at a redshift of 1.34 (Jackson et al. 1998). A spectroscopic survey discovered a group in the foreground of the lens, with 10 confirmed members and a mean redshift of $z = 0.29$ (Fassnacht & Lubin 2002). Further spectroscopic follow-up, presented in this paper, finds five more members.

2.2. *PG 1115+080*

This lens system (hereafter PG 1115), consisting of four lensed images of a $z_{\rm src} = 1.722$ quasar, was the second lens discovered (Weymann et al. 1980). The lens redshift is $z_{\rm lens} = 0.310$ (Kundić et al. 1997a; Tonry 1998). The system is especially important because it is one of only $\sim$10 lenses for which time delays have been measured (Schechter et al. 1997; Barkana 1997). Early observations of this system found a likely group of galaxies centered close to the lens system (Young et al. 1981) and found that two of the potential group members had redshifts of $\sim$0.3 (Henry & Heasley 1986), suggesting that the lensing galaxy was a member of a small group. The group membership was expanded by Kundić et al. (1997a) and Tonry (1998), who between them found five group members, including the lensing galaxy. Recent work by Momcheva et al. (2006) has extended the number of spectroscopically confirmed members to 13.

2.3. *JVAS B1422+231*

This is a four-image lens system (hereafter B1422) discovered by Patnaik et al. (1992a) as part as the Jodrell-VLA Astrometric Survey (Patnaik et al. 1992b; Browne et al. 1998; Wilkinson et al. 1998). The background source is at a redshift of $z_{\rm src} = 3.62$, while the lensing galaxy is at $z_{\rm lens} = 0.647$ (Hammer et al. 1995). Early models of the system (e.g., Hogg & Blandford 1994) suggested that external mass was necessary, and subsequent spectroscopy (Kundić et al. 1997b; Tonry 1998) revealed a group at the redshift of the lens. The work of Momcheva et al. (2006) has brought the number of spectroscopically confirmed group members to 16.

2.4. *CLASS B1600+434*

This two-image system (hereafter B1600) was one of the first two lenses discovered (Jackson et al. 1995) in the CLASS survey. The system redshifts are $z_{\rm src} = 1.59$ (Jackson et al. 1995)

and $z_{\rm lens} = 0.414$ (Fassnacht & Cohen 1998). This is another time delay system, with delays measured by Koopmans et al. (2000) at radio wavelengths and Burud et al. (2000) at optical wavelengths. A spectroscopic survey has discovered a small group with seven confirmed members that is associated with the lens (Auger et al. 2007).

2.5. *CLASS B1608+656*

This four-image system (hereafter B1608) was the second lens discovered (Myers et al. 1995) at the beginning of the CLASS survey. The lens redshift is $z_{\rm lens} = 0.630$ (Myers et al. 1995), while the source redshift is $z_{\rm src} = 1.39$ (Fassnacht et al. 1996). All three independent time delays in this system have been measured (Fassnacht et al. 1999, 2002). An extensive spectroscopic survey of the field has revealed four candidate galaxy groups along the line of sight to the lens, with mean redshifts of 0.26, 0.43, 0.51, and 0.63 (Fassnacht et al. 2006a). In this paper, we present new spectroscopy of the field and updated group velocity dispersions. As we discuss below, we concentrate on the properties of two of the groups in this field, the group that is physically associated with the lensing galaxy at $z = 0.632$ (hereafter B1608-1) and the group at $z = 0.426$ (hereafter B1608-3, using the notation of Fassnacht et al. 2006a).

2.6. *CLASS B2108+213*

This two-image system (hereafter B2108) has a lensing galaxy at $z_{\rm lens} = 0.365$ and has the largest image separation ($4.6''$) of the CLASS lenses (McKean et al. 2005), giving a strong indication that the lens resides in a group or cluster environment. Unusually, both the lensed source and the lensing galaxy are radio-loud, with the lensing galaxy showing both a flat-spectrum core and low surface brightness lobe extending in roughly an east-west to SE-NW direction (McKean et al. 2005; More et al. 2008). The source redshift has not yet been measured. A spectroscopic survey of the field has revealed several tens of galaxies at the redshift of the lens (J. P. McKean et al. 2008, in preparation).

3. X-RAY DATA REDUCTION AND ANALYSIS

3.1. *X-Ray Data Reduction*

In this section, we present results obtained from *Chandra* observations of the groups described in § 2. We report the first results for the groups associated with B0712 and B2108, while the data associated with the other groups have been obtained from the *Chandra* archive and reprocessed so that the full sample has been processed in an identical manner. We compare the results from the reprocessed data with those obtained from earlier work by Grant et al. (2004; for the PG 1115 and B1422 systems) and Dai & Kochanek (2005; for the B1600 and B1608 systems).

Observations of B0712 and B2108 were carried out with *Chandra*'s Advanced CCD Imaging Spectrometer (ACIS; Garmire et al. 2003) on 2003 December 17 (ObsID 4199) and 2006 July 14 (ObsID 6971), respectively. Both fields were imaged with the nominal 3.2 s CCD frame time, for a total integration of 45.5 ks for B2108 and 97.7 ks for B0712. The resulting data were transmitted in VFAINT mode for both observations. An examination of light curves produced from the data sets in the 0.3–10 keV band shows no indication of flaring during either observation. Both targets were imaged with the back-illuminated ACIS-S3 chip, with B0712 and B2108 located $44''$ and $75''$, respectively, from the aim point of the observation.

Data for the PG 1115, B1422, B1600, and B1608 systems were obtained from the *Chandra* archive maintained by the *Chandra* X-Ray Center.[1] The observational parameters for these data sets are listed in Table 1, along with those of the B0712 and B2108 observations. All of the archival fields were imaged with the ACIS-S3 chip near the telescope aim point, with the largest off-axis observation being that of B1608, imaged roughly $75''$ from the aim point. The observations of PG 1115 and B1422 were carried out in FAINT mode, while those of B1600 and B1608 are in VFAINT mode; all four employed the standard CCD frame time of 3.2 s. We searched for flaring events in the light curves of each observation using the `lc_clean.sl` script and detected periods of increased background in only the 367 data set of B1422. Excluding periods in which the background count rate differed from the mean rate by a factor greater than 1.5 reduced the usable exposure time of that observation from 28,429 to 16,888 s.

TABLE 1
OBSERVATION PARAMETERS

Target	ObsID	Exposure (s)	Observation Date	PI
B0712	4199	97742	2004 Dec 17	Fassnacht
PG 1115	363	26489	2000 Jun. 2	Garmire
B1422	367	16888[a]	2000 Jun. 2	Garmire
B1600	3460	30176	2003 Oct 7	Kochanek
B1608	3461	29717	2003 Sep 9	Kochanek
B2108	6971	45507	2006 Jul 14	Fassnacht

[a] Reduced from 28,429 s due to flaring events.

All six data sets were reprocessed and analyzed using standard *Chandra* Interactive Analysis of Observations (CIAO) version 3.3 software tools and version 3.2.2 of the *Chandra* calibration database available through the *Chandra X*-Ray Center. We produced new bad pixel masks for the 363, 367, and 4199 data sets with the `acis_run_hotpix` script, as the original masks were created by an older version of the *Chandra* pipeline that misidentified afterglow events and failed to detect hot pixels. New level 1 event files were produced for all of the observations using the `acis_process_events` script, which makes use of the latest gain files and corrects for the effects of time-dependent gain variations and charge transfer inefficiencies (CTIs) in the ACIS CCDs. To improve image quality, the preprocessing was implemented without event pixel randomization. Level 2 event files were produced by filtering on standard *Advanced Satellite for Cosmology and Astrophysics* (*ASCA*) grades (grades 0, 2, 3, 4, and 6), good status bits (status = 0), and Good Time Intervals (GTIs) supplied by the *Chandra* pipeline. To examine the extended emission originating from the galaxy groups associated with each system, we produced images in the soft X-ray band (0.5–2 keV), where emission from the intragroup gas would have the greatest signal. Each image was corrected for vignetting using exposure maps created at an energy of 1.5 keV. The pixel-specific vignette correction factor is estimated by normalizing the exposure map to its maximum value at the aim point of the observation. Images of the lens systems, binned to a pixel scale of $0.12''$, are shown in Figure 1. We note that the subpixel binning is used only to make Figure 1; all analysis is done with standard-size pixels.

3.2. *X-Ray Analysis*

In order to characterize the X-ray properties of the group sample, we must first remove any pointlike emission in the field of each system. This includes emission from the lensed active galactic

[1] See http://cxc.harvard.edu.

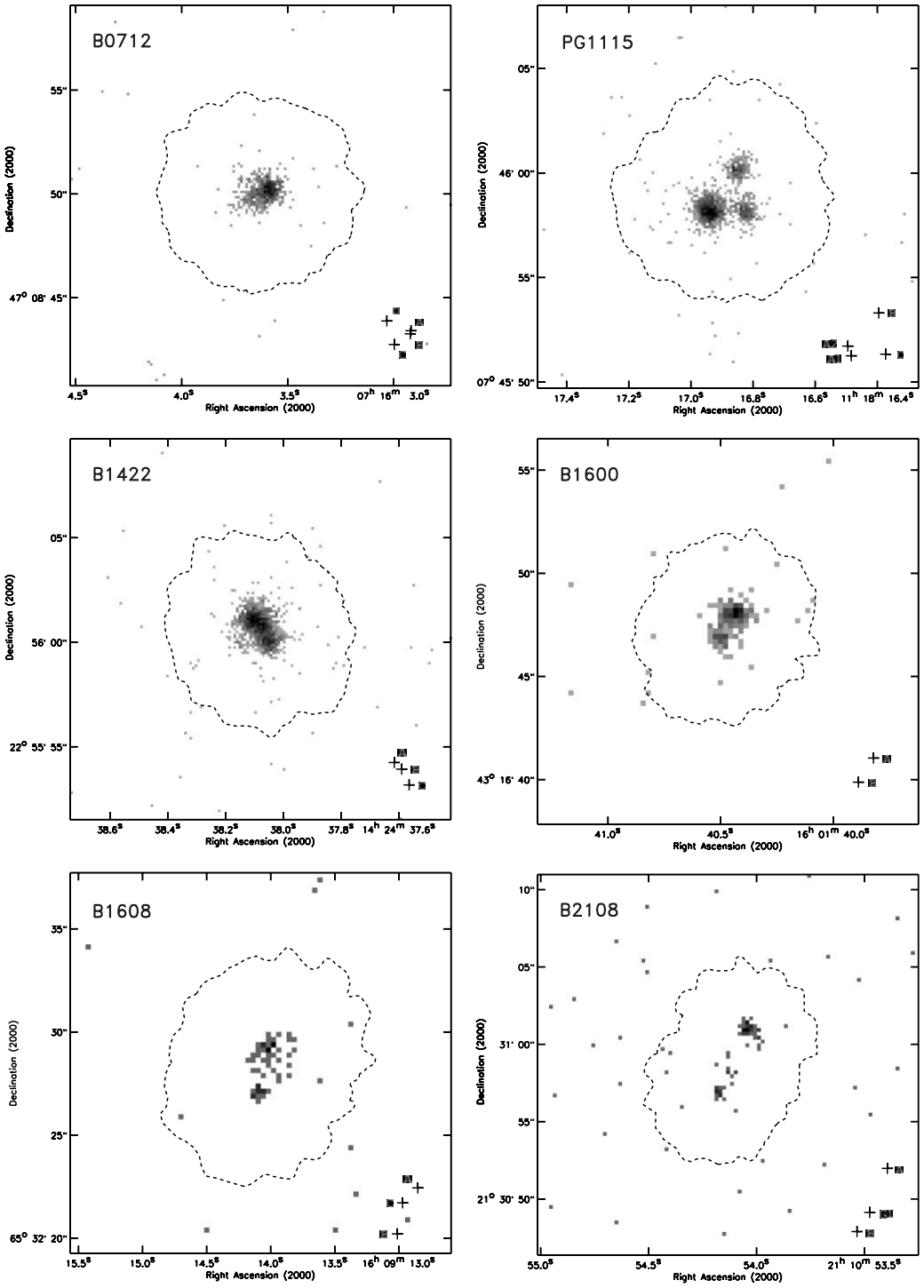

FIG. 1.—Soft-band (0.5–2.0 keV) X-ray images of the six lens systems, binned to a resolution of 0.123″. The dashed line denotes the masking aperture constructed to contain 99% of the flux from each set of point sources. The schematic in the lower right corner of each panel represents the configuration of the lens system at radio and optical wavelengths. For each case, a correspondence between the X-ray and optical/radio morphologies can be seen.

nuclei (AGNs) and possibly from the lensing galaxies, which are expected to be embedded in the fainter diffuse group emission. The excellent spatial resolution of *Chandra* facilitates the crucial separation of the point-source images from the underlying diffuse emission. Raw, soft-band images of the lens systems are shown in Figure 1. For each system, visual inspection reveals morphologies similar to those seen at other wavelengths, allowing the straightforward registration of the X-ray frame to the astrometry of the existing radio and optical data. In the B0712 system, the observed X-ray emission corresponds to the three brightest images of this quadruply lensed source, although the individual images are largely blended because their maximum separation is only 1.5″. The three components A, B, and C in PG 1115 are well separated, but the two images A1 and A2 have not been resolved. In B1422 we clearly see the blended emission from images A, B, and C, but not the fainter image, D. The B1600 morphology shows images A and B, while in B1608 the components A and C are blended, and only image B is well separated; image D is not

detected. The images of B1600 and B1608 match well the images presented by Dai & Kochanek (2005), as expected. In B2108 we see emission from both lensed images and the lensing galaxy (G1). The lensing galaxy in this system is therefore loud in both X-rays and radio.

Removing the contribution of these lensed images is complicated, as there is significant structure and signal in the wings of the *Chandra* point-spread function (PSF), even at low off-axis angles. Care must be taken to prevent residual flux in the wings from artificially enhancing any group component. While previous studies have used complex two-dimensional models to disentangle the pointlike and diffuse emission (Grant et al. 2004; Pooley et al. 2006), we have employed a relatively simple masking technique that uses PSF modeling to quantify the extent of point sources in each field and replace the point sources with an estimate of the local background. In order to minimize any contamination from the wings of the PSF, our masking apertures were constructed to contain 99% of the flux from a given point source. Using a process similar to that employed by the ACIS Extract[2] package, model PSFs were constructed using the CIAO tool `mkpsf` at an energy of 1.5 keV. As the *Chandra* PSF is dependent on the off-axis angle, a unique PSF was constructed for each lensed image. Once the X-ray data had been registered to the optical and radio frames, the positions of the lensed components were taken from the literature and used as the centroids for the masking apertures. We draw from the 5 and 8.4 GHz radio observations of Jackson et al. (1998), Patnaik et al. (1999), Fassnacht et al. (2002), and McKean et al. (2005) for B0712, B1422, B1608, and B2108, respectively, and from the *Hubble Space Telescope* (*HST*) optical observations of Impey et al. (1998) for PG 1115. Each model PSF is then convolved with a two-dimensional Gaussian with $\sigma = 0.27''$ to account for the telescope dither blur,[3] and a 99% enclosed energy contour is constructed from the smoothed image. The outer extent of the combined contours for a set of lensed images is then defined as our masking aperture for that system. These masking regions are shown plotted on their respective fields in Figure 1. A local background is then determined directly outside the masking aperture, and the masked region is filled with the median background level, scaled to the area of the masked region, using the `dmfilth` task.

The images were next smoothed in order to emphasize the diffuse X-ray emission associated with these systems. Both adaptive smoothing, using the CIAO tool `csmooth` (Ebeling et al. 2006), and fixed-width Gaussian smoothing techniques were used. The results are shown in Figure 2. The middle two columns of the figure show the adaptively smoothed images of each system prior to and following the masking process. In many of the fields a diffuse component is clearly visible even with the lensed images present. After masking these sources, we applied the adaptive smoothing algorithm with minimum and maximum significance thresholds of 3 and 5 σ, respectively. The minimum and maximum smoothing scales were allowed to float. An examination of the resulting images showed diffuse emission in four of the six fields: B0712, PG 1115, B1422, and B2108. On the other hand, we see no obvious signal in the fields of B1600 and B1608, in agreement with the results of Dai & Kochanek (2005), who also fail to detect any significant extended emission within $4'$ of the lens galaxies. In the B1608 field, we do notice a region of enhanced emission near the location of the B1608-3 group. However, this location is close to the chip edge, and it is not clear whether the emission is real or due to a higher background level. Deeper X-ray observations are needed to assess whether the B1608-3 group has associated diffuse X-ray emission.

The rightmost column of Figure 2 shows the masked data smoothed by a fixed-width Gaussian with a kernel size of $20''$. For all but one of the lens systems, the fixed-width smoothing produces an image that strongly resembles the image produced from the adaptive smoothing. This is clearly not the case for the B2108 field, where the fixed-width smoothing reveals at least two major components. The difference between the adaptive and fixed-width smoothing results may be due to the bridge of relatively bright emission connecting the two components. We believe that the adaptive smoothing algorithm probably detected the two components plus the bridge as a single large object and thus incorrectly smoothed the data with a very large kernel size. To assist in the interpretation of the smoothed images, we binned the raw masked data to $16''$ pixels. The binned imaged shows a somewhat U-shaped structure that more closely resembles the Gaussian-smoothed image than the adaptively smoothed image. We therefore feel that for B2108 the fixed-width smoothing has probably produced a more accurate representation of reality. We will, thus, use the Gaussian-smoothed image in the following discussion. We designate the western component, which is the one roughly centered on the lens system, as B2108-1. The eastern component is referred to as B2108-2.

The majority of the quantitative results, such as the total counts, fluxes, etc., that are presented below are derived from the masked unsmoothed images. However, the smoothed images are used to determine the centroids of the diffuse X-ray emission. Because we feel that the fixed-width Gaussian smoothing produces a more realistic representation of the B2108 emission and because the fixed-width smoothing also seems reasonable for the other lens fields, we use the Gaussian smoothing to determine the centroids for all of the fields. The resulting centroids are listed in Table 2. It is worth noting that the lack of structure in the smoothed images of B1600 and B1608 suggests that there is no significant residual flux or artifact produced as a result of the masking process itself; we proceed under the assumption that this holds true for the other four fields as well.

It was not possible to do a full spectroscopic analysis for any of the fields, due to the low number of counts produced by the diffuse emission. Although an analysis of the B2108-1 system, which has the highest number of counts among the detected systems, did yield a temperature, the uncertainties were so large as to render the value meaningless. Therefore, we instead determined the soft-band flux of the group emission by normalizing a Raymond-Smith spectral model in the CIAO package Sherpa to the net counts detected above the background in each system. The net counts were measured using a standard growth curve analysis, although the analysis of B2108 was more complex than that of the other systems. For all but the B2108 system, the local background levels were determined by creating azimuthally averaged surface brightness profiles. For the systems with detected diffuse emission, the annuli were centered on the peak of the emission. For the B1600 and B1608 systems the annuli were placed at the group centers as determined from optical observations. The background for each system was set to the median surface brightness in the region where the profile leveled off. The widths of the annuli were held constant for a given system, but varied between $5''$ and $10''$ from field to field, depending on the achieved signal-to-noise ratio of the detected diffuse emission. The surface

[2] See Broos, P., Townsley, L., Getman, K., & Bauer, F. 2002, ACIS Extract, An ACIS Point Source Extraction Package (University Park: Pennsylvania State Univ.), http://www.astro.psu.edu/xray/docs/TARA/ae_users_guide.html.

[3] See Broos, P., Townsley, L., Getman, K., & Bauer, F. 2002, ACIS Extract, An ACIS Point Source Extraction Package (University Park: Pennsylvania State Univ.), http://www.astro.psu.edu/xray/docs/TARA/ae_users_guide.html.

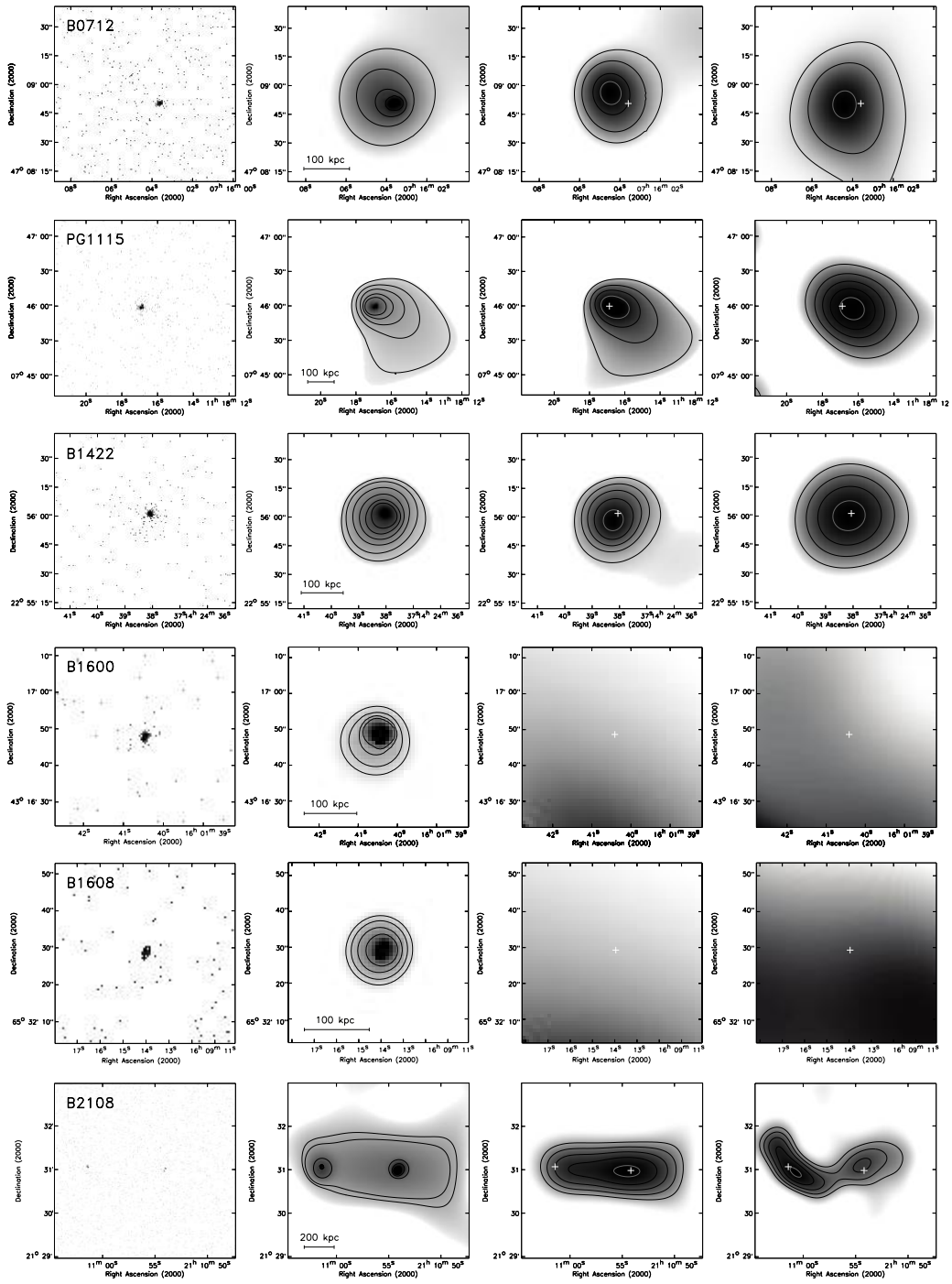

FIG. 2.—Col. (1): Raw soft-band (0.5–2.0 keV) X-ray images binned to a pixel scale of 0.492″ of the field of each galaxy group. Col. (2): Adaptively smoothed images of each system prior to the masking process. Col. (3): Adaptively smoothed images of each system following the masking process. The position of the masked point sources are marked with plus signs. The flaring seen on the right edge of the B2108 adaptively smoothed image is due to the chip edge. Col. (4): Same as col. (3), but smoothed with a fixed-width 20″ Gaussian kernel. The contour levels in the smoothed images are chosen to highlight the important structures. The scale bars in the second column are drawn under the assumption that $h = 0.7$.

brightness profiles are shown in Figures 3 and 4. In the case of the two components seen in the B2108 field, the standard approach could not be used because the complex morphology of the emission produces cross-contamination of the group counts. Therefore, instead of using surface brightness profiles, we set the background level by measuring the surface brightness in a source-free area of the chip.

A cumulative net count profile for each field was constructed by measuring the counts in successively larger apertures centered on the group emission and subtracting an appropriately scaled background. We take the total number of counts originating from the group to be the level at which the cumulative profile ceases to grow. In the case of the B2108 components, it was necessary to mask out parts of the apertures where the counts from the group in question were significantly contaminated by the emission from the other group. Figure 5 shows the masking regions used, and Figure 6 shows the resulting curves of growth. The total counts measured in each system are listed in Table 2, where the counts from the B2108 are underestimates due to the masking procedure. We find significant signal above the background for the B0712,

TABLE 2
X-RAY PROPERTIES OF DIFFUSE GROUP EMISSION

Group (1)	R.A. (J2000.0) (2)	Decl. (J2000.0) (3)	N_H (10^{20} cm^{-2}) (4)	Net Counts (5)	Count Rate (10^{-3} s^{-1}) (6)	Flux[a,b] (10^{-15} ergs cm^{-2} s^{-1}) (7)	$L_{X,bol}$[b] (10^{42} h^{-2} ergs s^{-1}) (8)	$L_{X,bol,500}$[b] (10^{42} h^{-2} ergs s^{-1}) (9)
B0712.....	07 16 04.4	+47 08 49	7.8	47	0.48	1.6 ± 0.2	0.44 ± 0.05	1.3 ± 0.2
PG 1115	11 18 16.3	+07 45 57	4.0	71	2.7	6.9 ± 0.8	2.2 ± 0.3	3.9 ± 0.5
B1422.....	14 24 38.1	+22 56 00	2.7	59	3.5	9 ± 1	3.4 ± 0.5	12 ± 1
B1600.....	...	...	1.3	...	...	<1.8	<1.2	<1.2
B1608-1.....	...	...	2.7	...	...	<2.0	<4.0	<4.0
B1608-3.....	...	...	2.7	...	...	<4.3	<3.0	<3.0
B2108-1.....	21 10 54.4	+21 31 05	12.6	155	3.4	12 ± 1	5.9 ± 0.5	5.9 ± 0.5
B2108-2.....	21 11 00.7	+21 30 55	12.6	148	3.3	11 ± 1	5.4 ± 0.5	...

NOTE.—Units of right ascension are hours, minutes, and seconds, and units of declination are degrees, arcminutes, and arcseconds.
[a] 0.5–2.0 keV.
[b] Corrected for Galactic absorption.

PG 1115, B1422, and B2108 systems, with the emission in the B0712 detected at the 3.5 σ level and all the other systems detected at the 4.5–5 σ level. We did not detect significant emission in the B1600 and B1608 systems, confirming our nondetection in these fields from the image analysis. As discussed below, the fluxes we present for the B1600 and B1608 systems are 3 σ upper limits.

For the four fields with detected diffuse emission, we converted from net counts to flux by modeling the group emission in Sherpa as a Raymond-Smith thermal plasma with a metal abundance of 0.3 $Z_\odot$ and a gas temperature of 1 keV. The instrument response is taken into account by creating redistribution matrix and auxiliary response files with the `specextract` task for each observation. Using these response matrices and the Raymond-Smith model, along with the redshift for the groups and the exposure times of the observations, we determined the source flux required to produce the observed counts in each field. These fluxes were then corrected for the effects of Galactic absorption using the neutral hydrogen column densities of Dickey & Lockman (1990). Finally, these fluxes were converted to rest-frame soft-band luminosities and then to rest-frame bolometric luminosities. The computed fluxes and luminosities are given in columns (7) and (8) in Table 2.

For ease of comparison with other determinations of group X-ray properties, we also computed values within apertures of radius R_{500}. The value of R_{500} for each system was estimated from the radial velocity dispersion that had been determined from the group galaxy redshifts (Table 3), as $R_{500} = 2\sigma_v/[\sqrt{500}H(z)]$. For each group, we had to extrapolate from the region of observed emission out to R_{500}. To do this, we used a β-model with $\beta = 2/3$ and $R_{core} = 160$ kpc; these are the median and mean values, respectively, from the fits to the intermediate-redshift group sample of Jeltema et al. (2007). The rest-frame bolometric luminosity within R_{500} is given in column (9) Table 2. To obtain upper limits on the flux in the fields of B1600 and B1608, we used a similar process, but instead normalized the spectral models to the background counts within apertures of radius R_{500} centered on the lensed images. The values listed in Table 2 for these three groups are the 3 σ upper limits within these apertures.

4. OPTICAL DATA REDUCTION AND ANALYSIS

In order to compare the X-ray and optical properties of the group sample, we require estimates of the group velocity dispersions. As we did for the X-ray properties, we calculate the velocity dispersions for all the groups using a standardized approach in order to minimize effects due to different computation methods. To do this, we took the updated redshift distributions for the PG 1115 and B1422 systems from Momcheva et al. (2006) and the B1600 redshift information from Auger et al. (2007). Furthermore, we supplemented the previously existing redshift data on B0712 from Fassnacht & Lubin (2002) and on B1608 from Fassnacht et al. (2006a) with new data that we present below. Finally, we included the preliminary analysis of the data for the

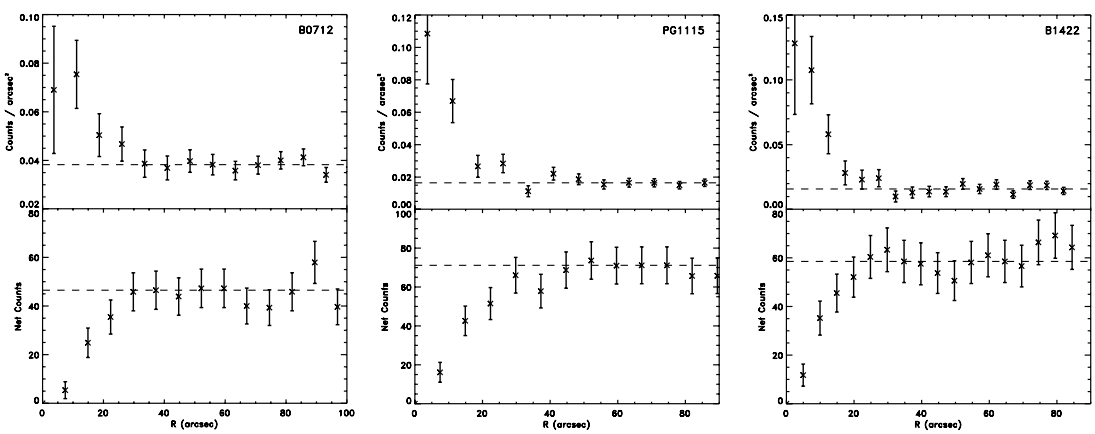

FIG. 3.—*Top*: Azimuthally averaged surface brightness profiles for the B0712, PG 1115, and B1422 groups, constructed following the masking of point sources in the field. The background level of each field is denoted by the horizontal dashed line. *Bottom*: Cumulative net count profiles for each system detected above the background. The total number of counts originating from each group is shown by the horizontal dashed line.

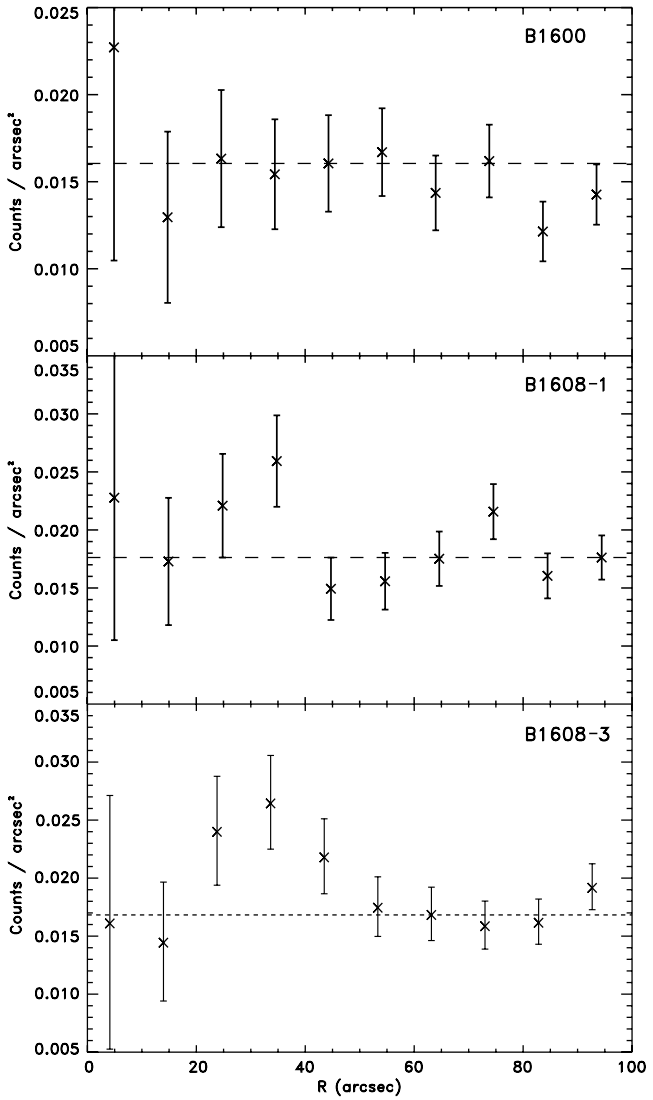

FIG. 4.—Azimuthally averaged surface brightness profiles for the B1600 and B1608 fields. Because no significant diffuse emission is detected at these locations, the profiles are centered on the optical centroids of the groups.

B2108 field. These data will be presented fully by J. P. McKean et al. (2008, in preparation).

4.1. *B0712 Spectroscopy*

Previous observations of the environment of the B0712 field yielded 34 nonstellar redshifts, with 10 galaxies comprising the foreground group (Fassnacht & Lubin 2002). We obtained further spectroscopy on the field on 2004 April 10 with the Low Resolution Imaging Spectrograph (LRIS; Oke et al. 1995) on the Keck I Telescope. The observations consisted of three multislit exposures of 1800 s each. Arc lamp and internal flat-field exposures were obtained following the science exposures. The data were obtained with both the red and blue LRIS cameras, with the D560 dichroic splitting the incoming beam at ~5700 Å. The red-side data were dispersed by the 600/7500 grating, giving a nominal scale of 1.28 Å pixel^{-1}. On the blue side, the 400/3400 grism was used, providing a nominal 1.09 Å pixel^{-1} dispersion. The data were reduced with a python-based multislit reduction package developed by M. Auger. This package detects the slits, does the bias subtraction and flat-field correction, corrects for distortions in the spatial direction, does the wavelength solution, rectifies the spectra, subtracts the sky, detects objects in each slit, and extracts the spectra, all automatically. The slit mask had 32 slits, from which 13 nonstellar spectra were extracted. The updated redshift distribution is shown in the left panel of Figure 7.

4.2. *B1608 Spectroscopy*

The spectroscopic data on the B1608+656 field that are presented in Fassnacht et al. (2006a) yielded 97 nonstellar redshifts in a distribution that showed four clear spikes. Additional multislit observations of the field were obtained on 2004 August 13 and 2007 June 12, with one slit mask being used on each occasion. In both cases, both red- and blue-side data were obtained. The first set of observations used the D560 dichroic, the 600/7500 red-side grating, and the 600/4000 blue-side grism, yielding nominal dispersions of 1.28 and 0.63 Å pixel^{-1} for the red and blue sides, respectively. Two 1800 s observations were obtained. The second set used the D680 dichroic, the 831/8200 grating, and the 300/5000 grism. This combination provided nominal dispersions of 0.93 and 1.43 Å pixel^{-1}. This second set of observations

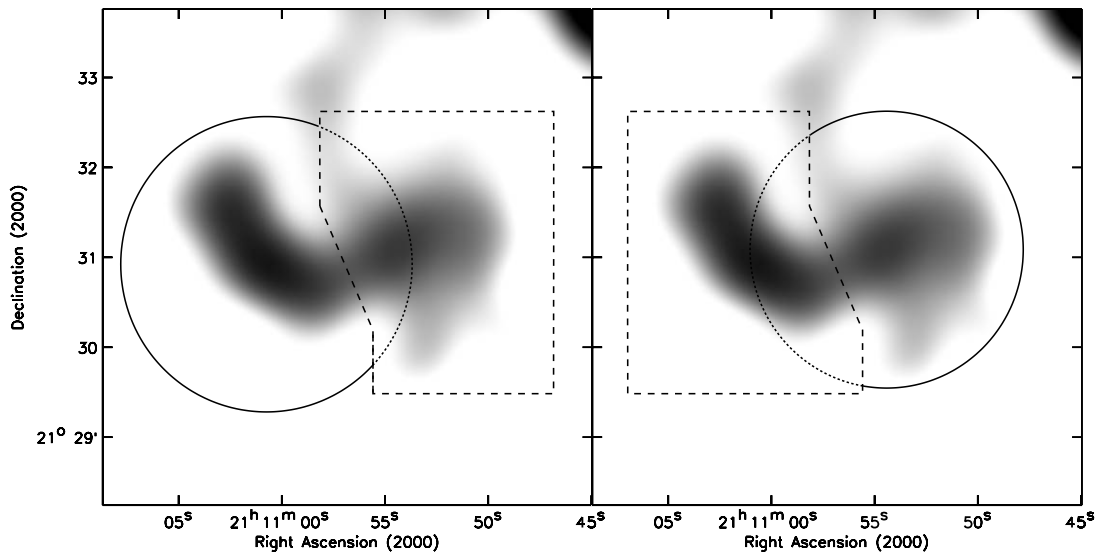

FIG. 5.—Gaussian-smoothed images of the B2108 field showing the masking regions (*dashed polygons*) used to minimize the cross-contamination of the counts associated with each component. Counts in these masking regions were excluded when measuring the cumulative net profiles of the components. The circle in each panel is centered on the component for which the counts are being measured and shows the radius at which the background level was reached.

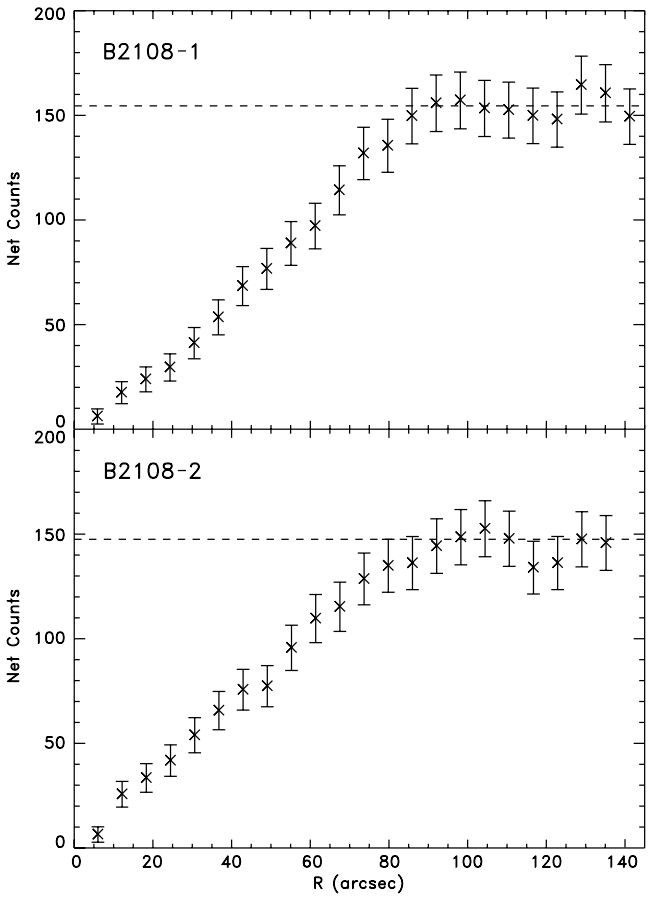

FIG. 6.—Cumulative net count profiles for the two regions of diffuse emission in the B2108 field. The masking that was applied to reduce cross-contamination between the groups leads to underestimated count levels in the outer regions of the profiles.

was designed to measure an improved stellar velocity dispersion for the B1608 primary lensing galaxy and to make the first measurements of the stellar velocity dispersions of the two additional strong lens candidates in this field (Fassnacht et al. 2006b), so the total exposure times were long. In total, 11 exposures of length 1800 s were obtained through this mask. Both masks were reduced using the automated python pipeline. The observing conditions during the 2004 observations were substandard, and only two new redshifts were measured from the mask. In contrast, 26 new nonstellar redshifts were measured from the 2007 observations. The updated redshift distribution is shown in the right panel of Figure 7.

4.3. *Optical Analysis*

In order to minimize the likelihood of spurious conclusions arising from different data analysis methods, we computed the group velocity dispersions for each of the systems in the same way. In some cases (B1422 and PG 1115), this means reanalyzing the data from the literature, while for others (B0712, B1608, and B2108) we acquired new data that have been combined with previously published data, if available. For the B1600 group, the published group parameters (Auger et al. 2007) were computed using our standardized technique, and therefore they were taken directly from the literature. The first step is to identify the groups from the redshift distributions. To do this, we follow the iterative group-finding procedure presented in Auger et al. (2007). In some cases, this objective method leads to a slightly different membership than that presented in the literature. The number of galaxies given for each of the groups in Table 3 reflects the numbers from the current analysis. We note that for the B1608 field, the objective group finder identifies the same four redshift spikes as noted in Fassnacht et al. (2006a) plus an additional group candidate at $z = 0.71$. However, we consider only two groups in our analysis, the one that is physically associated with the lensing galaxy (B1608-1) and the $z = 0.426$ group (B1608-3). Both of these groups are compact spatially and in redshift, and are clearly centered in the region covered by our data. In contrast, the $z = 0.26$ group appears to be real, but it also has a spatial distribution that suggests that it may be centered off the region covered by the spectroscopic and X-ray data. The $z = 0.52$ spike has a filamentary spatial distribution and is composed mostly of late-type galaxies, so we do not believe that it is a real group. The new $z = 0.71$ candidate has too few members for us to accurately characterize its properties at this time and is also so distant that the relatively shallow *Chandra* data do not provide interesting constraints on its properties.

The velocity dispersions were calculated from the distributions of the redshifts of the identified group members, using the methods described in Beers et al. (1990). The gapper algorithm was used for groups with fewer than 15 members, while for groups with more members we used the biweight estimator. In each case, the errors on the resulting velocity dispersions were determined using a bootstrap approach. The dispersions and their errors are given in Table 3. Although the group velocity dispersions have been calculated in a standard manner, we note that a dispersion

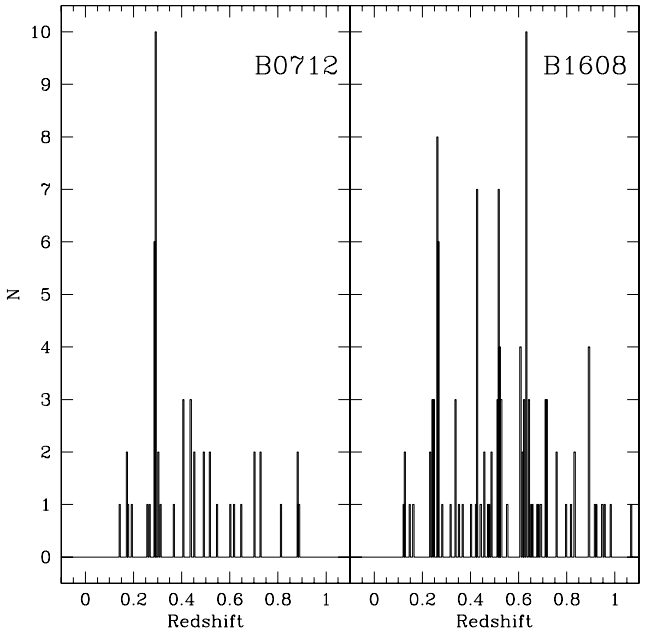

FIG. 7.—Galaxy redshift distributions in the B0712 (*left*) and B1608 (*right*) fields. The bins have width $\Delta z = 0.005$.

TABLE 3
GROUP OPTICAL PROPERTIES

Group	N	Group Redshift	σ_v (km s^{-1})	R_{500} (h^{-1} kpc)	θ_{500} (arcsec)
B0712.....	15	0.290	320 ± 20	250	82
PG 1115.....	13	0.310	450 ± 70	340	110
B1422.....	16	0.339	460 ± 90	350	105
B1600.....	7	0.415	90 ± 20	72	19
B1608-1.....	10	0.632	150 ± 30	95	20
B1608-3.....	8	0.426	320 ± 90	190	49
B2108.....	47	0.364	470 ± 50	350	98

determined from only ∼10 members may be strongly biased with respect to the true value (e.g., Zabludoff & Mulchaey 1998; Gal et al. 2007), and thus the calculated values should be used with care.

5. DISCUSSION

5.1. *Comparison to Previous X-Ray Analyses*

The diffuse X-ray emission from two of the lens-selected groups, PG 1115 and B1422, has been analyzed previously by Grant et al. (2004). Because our analysis uses different inputs and techniques, care should be taken when comparing the results of the two analyses. For one example, each of these two systems was observed under two separate programs (ObsIDs), namely, 363 and 1630 for PG 1115 and 367 and 1631 for B1422. To simplify the analysis of the effects of the PSF, we used only the longer of the two observations for each system. In contrast, the Grant et al. (2004) analysis combined the two programs in each case. Therefore, the germane basic quantity to use in the comparison of the results is not the net counts from the diffuse emission, but rather the net count rates. In each case, we find a higher count rate than that measured in the previous analysis, 2.7×10^{-3} versus 1.3×10^{-3} for PG 1115 and 3.5×10^{-3} versus 1.8×10^{-3} for B1422, where all values are in counts s^{-1}. We believe that the cause of this discrepancy is the manner in which we masked out the lensed AGN emission for the lenses. The Grant et al. (2004) approach was conservative, masking out regions with diameters of 14″–16″, while our 99% masking regions (Fig. 1) cover somewhat smaller areas, with typical sizes of ∼10″ across. In both cases, a correction was then made to account for the diffuse flux within the masked region. Given the small angular extent of the groups, changes in the masking area may lead to differences in the size of the correction and therefore to significant changes in the measured flux of the diffuse emission.

A second difference in technique is that the luminosities that we use in our final analysis are those within R_{500}, rather than using just the luminosities calculated from the observed region of significant detection. To facilitate comparison with the Grant et al. (2004) results, the bolometric rest-frame luminosities in Table 2 are given for both the detection region and the R_{500} region. Other differences arise from the X-ray temperature used for PG 1115, for which Grant et al. (2004) use 0.7 keV and we use 1.0 keV, and the assumed cosmology. The Grant et al. (2004) results are computed using an Einstein–de Sitter cosmology with $h = 0.5$, while we use $(\Omega_m, \Omega_\Lambda) = (0.3, 0.7)$ and set $h = 0.7$ when we have to fix its value.

It is important to consider the effects that the analysis techniques have on the interpretation of the results. In terms of many of the conclusions drawn from the measured X-ray luminosities, including the discussion of the L_X-σ_v relationship below, the factors of a few in L_X that come out of the different techniques do not change the interpretation. In particular, given the log-log nature of the L_X-σ_v plot and the scatter in the observed relationship, these factors of 2–3 do not significantly change the location of the lens group points in Figure 8. On the other hand, the determination of the location of the X-ray centroid is more sensitive to how the lensed AGN emission is masked, and therefore conclusions about the possible offsets of the brightest group galaxies from the center of the X-ray emission are tentative at best.

5.2. *The Nature of the X-Ray Emission in B2108*

The X-ray emission associated with the B2108 system is shown in the bottom row of Figure 2, where its morphology is seen to be clearly different from that of the other systems. While the smoothed data in each of the other fields show a single, relatively compact region, the B2108 field contains two elongated regions, connected by a bridge of emission. These regions are roughly centered on the positions of masked point sources; the western component (B2108-1) is the one centered on the lens system.

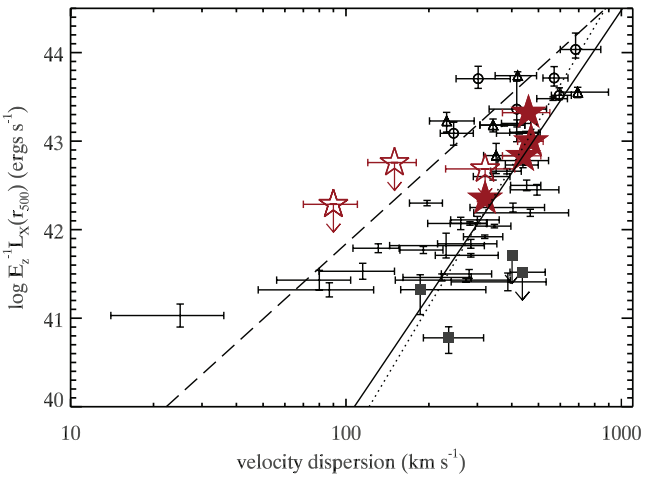

FIG. 8.—L_X-σ_v plot showing moderate-redshift lens-selected groups from this paper (*large stars, with open stars representing upper limits*), low-redshift X-ray–selected groups from GEMS (Osmond & Ponman 2004; *error bars with no points*), moderate-redshift X-ray–selected groups from Jeltema et al. (2006; *circles*) and Willis et al. (2005a; *triangles*), and low-redshift optically selected groups from the Two Degree Field Survey (2dF; Rasmussen et al. 2006; *squares*). The solid line represents the fit to the GEMS sample (S. F. Helsdon & T. J. Ponman 2008, in preparation), while the dotted line is the fit to the low-redshift cluster data of Markevitch (1998) and Horner (2001). The long-dashed line is a fit to a sample of intermediate-redshift groups and clusters (Gastaldello et al. 2008).

It is likely that the X-ray emission in B2108-1 is produced by the group associated with the B2108+213 lens system. The lensing galaxy is a massive elliptical, is the brightest galaxy in the group, and is found nearly at the center of the X-ray emission. However, the source of emission in B2108-2, the eastern X-ray component, is much less clear. An examination of optical imaging of this field, obtained with the Keck telescope, shows a $R > 23$ source coincident with the X-ray position of the point source that is roughly at the center of B2108-2. The faintness of this optical object compared to the confirmed group members (∼5 mag fainter than the primary lensing galaxy) suggests that it is a background AGN, rather than a source associated with a massive elliptical in the $z = 0.36$ group. If this is the case, then it is not clear whether the diffuse X-ray emission in B2108-2 is coming from a massive system associated with a background AGN or whether it is instead due to a second group at the redshift of the lensing galaxy. The clear removal of the point-source emission for the B1600 and B1608 systems suggests that the diffuse emission is not wholly due to residual emission from the point source. The majority of the B2108-2 emission is outside the region for which spectroscopic data have been obtained, so there is no information on whether there may be an overdensity of higher redshift objects in the area covered by this second system. That being said, the available spectroscopy does provide some insights regarding this complex field. The velocity distribution of the $z = 0.36$ group members is non-Gaussian, even with nearly 50 redshifts (J. P. McKean et al. 2008, in preparation), suggesting that the group is in a dynamically disturbed state. The velocity distribution in the B2108 field and the presence of multiple elongated diffuse components connected by an apparent bridge of emission suggest that this system is undergoing some kind of merger. Interestingly, the east-west alignment of the two diffuse X-ray components is roughly in the same direction as the

low surface brightness lobes seen in deep radio imaging of this system (More et al. 2008), although the radio lobes cover a much smaller area than the X-ray emission.

5.3. *Detection Rate and Group Luminosities*

One of the most basic quantities that emerges from the analysis of the lens group sample is the rate at which these lens-selected groups are detected when observed at X-ray frequencies. We have examined the fields of six lenses, in which at least seven galaxy groups have been discovered using optical spectroscopy. Of those seven groups, four are detected with the *Chandra* observations, giving a formal detection rate of $\sim$60% $\pm$ 30%. All of the detected lens-selected groups have luminosities within R_{500} of greater than $10^{42}\,h^{-2}$ ergs s^{-1}. Because most previous investigations of the X-ray properties of galaxy groups have been conducted at low redshifts, we compare the rate at which X-ray emission from the IGM is detected in the lens sample to these samples. Mahdavi et al. (2000) selected groups and clusters based on the CfA redshift survey and found a detection rate of 23%, which they correct to a 40% rate based on their X-ray selection function. The X-ray data used for this work were from the *Röntgensatellit* (*ROSAT*) All-Sky Survey (RASS; Voges et al. 1999) and thus are not highly sensitive, with a limiting luminosity of $\sim 10^{42}$ ergs s^{-1}. Osmond & Ponman (2004) concentrate more specifically on groups and detect $\sim$60%, based on deeper pointed X-ray observations with *ROSAT*. For this sample, the limiting luminosity is $L_X \sim 10^{41}$ ergs s^{-1}. However, analysis and sample selection issues make a straight comparison of detection rates in these earlier samples somewhat problematic. The shallow X-ray data used in Mahdavi et al. (2000) make it difficult to disentangle IGM emission from emission due to a hot halo associated with one of the group galaxies (e.g., Mulchaey 2000; Osmond & Ponman 2004). The Osmond & Ponman (2004) sample avoids this problem by using deeper *ROSAT* pointings, but their sample may be biased. Their groups are optically selected, but they require their groups to have preexisting deep ($t_{\rm exp} > 10,000$ s) *ROSAT* data, which were often available because the RASS data had shown an X-ray source at that location.

Perhaps the best comparison sample for our lens-selected groups is the work on local optically selected groups by Rasmussen et al. (2006). Here the selection is unbiased, at least with respect to the X-ray properties, and the X-ray observations, which are made with *XMM-Newton*, are sensitive. The IGM has been detected in two of the four groups, giving a similar detection rate to the lens-selected samples. We note, however, that none of the groups in this sample have luminosities above $10^{42}\,h^{-2}$ ergs s^{-1}. Although both the lens group and Rasmussen et al. (2006) samples are small, we may be seeing a difference in the sample properties. The optically selected sample may be more representative of typical low-redshift galaxy groups, which often have low levels of X-ray emission. In contrast, the lens-selected sample is picking out groups that are more like the X-ray–bright groups detected in local samples, which tend to be on the high-mass side of the local group distributions (e.g., Mahdavi et al. 2000; Mulchaey & Zabludoff 1998).

5.4. L_X-σ_v *Relationship*

In order to compare the properties of the X-ray emission from the lens-selected moderate-redshift groups with other group samples, we have assumed $h = 0.7$ and $(\Omega_m, \Omega_\Lambda) = (0.3, 0.7)$. The lens group points are plotted as the large stars on the L_X-σ_v plot in Figure 8. For the purposes of this plot, we have assumed that all of the measured redshifts in the B2108 field are associated with the B2108-1 group and plotted the derived velocity dispersion against the B2108-1 X-ray luminosity. Also included in the plot are data from the low-redshift X-ray–detected groups in the GEMS sample of Osmond & Ponman (2004) and from X-ray–selected moderate-redshift group samples (Jeltema et al. 2006; Willis et al. 2005a). The squares represent data on the four groups from Rasmussen et al. (2006). As mentioned above, these optically selected groups appear to be less X-ray luminous than typical systems in the X-ray–selected samples (Fig. 8). In contrast, the lens-selected groups appear to be consistent with the X-ray–selected samples, given the scatter in the data.

Also shown in Figure 8 are fits to low- and intermediate-redshift samples. The low-redshift scaling relations are shown for the GEMS group sample (*solid line*; S. F. Helsdon & T. J. Ponman 2008, in preparation) and a cluster sample (*dotted line*; Markevitch 1998; Horner 2001). The other scaling relation (*dashed line*) in the plot is a fit made by Gastaldello et al. (2008) to data from an intermediate-redshift group sample, the majority of which is comprised of the Jeltema et al. (2006) and Willis et al. (2005a) data points represented, respectively, as the circles and triangles in Figure 8. It is clear that the lens group detections are more consistent with the low-redshift scaling relations than the intermediate-redshift relation. However, Gastaldello et al. (2008) do point out that their fitted slope may not be representative of the true relation because the velocity dispersion measurements may be biased low. Of course, it is difficult to draw strong conclusions from only four detections in the lens group sample, but the upper limits, while not constraining the properties of the lens-selected sample in a meaningful way, are still perfectly consistent with the low-redshift scaling relations and marginally consistent with the intermediate-redshift scaling relation. It should be noted that the three lens-selected groups that were not detected all lie at $z > 0.4$, while the four that were detected all have $z < 0.4$. Deeper X-ray observations of the B1608 and B1600 fields, which now each have only $\sim$30 ks of *Chandra* data, would enhance the conclusions that can be drawn from the lens group sample.

5.5. *BGG Offsets*

In low-redshift samples, the brightest group galaxy (BGG) is nearly always located at the spatial and dynamical center of the group (e.g., Zabludoff & Mulchaey 1998), and the diffuse X-ray emission from the group is also centered on the BGG (e.g., Mulchaey & Zabludoff 1998; Helsdon & Ponman 2000; Osmond & Ponman 2004). The coincidence between the diffuse X-ray gas and the BGG becomes less prominent in samples of X-ray–selected moderate-redshift groups, where some groups have negligible BGG offsets but others have offsets up to $\sim 160\,h^{-1}$ kpc (Jeltema et al. 2006, 2007). The lens-selected systems presented in this paper span a redshift range similar to the Jeltema et al. (2007) sample and thus provide an interesting comparison sample. We have identified the brightest spectroscopically confirmed member of each of the groups for which diffuse X-ray emission has been detected, either from our own imaging (for B0712 and B2108) or from the data in Momcheva et al. (2006; for PG 1115 and B1422). The X-ray centroids are derived from the Gaussian-smoothed images in the last column of Figure 2. For the B2108 field, we calculate the offset between the BGG and the centroid of B2108-1. The offsets between the BGGs and the X-ray centroids are given in Table 4, and overlays of the X-ray contours on *HST* images are shown in Figure 9. For B2108 the BGG is also the lensing galaxy. However, in B0712 (because the group lies at a lower redshift than the lens), PG 1115, and B1422 the lens is not the BGG. Therefore, Table 4 also gives the offsets between the lensing galaxies and the X-ray centroids.

The offsets between the centroids of the diffuse X-ray emission and the BGGs are small to moderate, with all of the offsets

TABLE 4
Offsets from X-Ray Centroid

Lens System	BGG R.A. (J2000.0)	BGG Decl. (J2000.0)	Offset (arcsec)	Offset (h^{-1} kpc)	Lens Galaxy R.A. (J2000.0)	Lens Galaxy Decl. (J2000.0)	Offset (arcsec)	Offset (h^{-1} kpc)
B0712	07 16 05.01	+47 09 04.8	16	49	07 16 03.58	+47 08 50.0	9[a]	[a]
PG 1115	11 18 15.52	+07 45 47.7	16	51	11 18 17.00	+07 45 57.7	10	31
B1422	14 24 38.39	+22 55 53.5	7	24	14 24 38.09	+22 56 00.6	1	3
B2108-1	21 10 54.03	+21 31 00.4	7	25	21 10 54.03	+21 31 00.4	7	25

Note.—Units of right ascension are hours, minutes, and seconds, and units of declination are degrees, arcminutes, and arcseconds.
[a] The lens is not physically associated with the group.

being $\leq 20''$. At the redshifts of these groups, $z \sim 0.3$–0.4, these offsets correspond to physical distances of ~ 25–$50\ h^{-1}$ kpc. For comparison, five out of the seven groups in the sample of Jeltema et al. (2007) had BGG offsets of $< 15\ h^{-1}$ kpc, while the other two had offsets of 110–160 h^{-1} kpc. In spite of the BGG–X-ray offsets measured in the lens group sample, we cannot yet conclude that this sample is similar in character to the Jeltema et al. (2007) one. This is because slight changes in analysis techniques can lead to significant changes in the centroid position of lens-selected groups, as can be seen by comparing our X-ray images of PG 1115 and B1422 to those in Grant et al. (2004). Even with the excellent angular resolution of *Chandra*, the determination of the morphology of faint diffuse emission in the presence of bright lensed AGN images is challenging. Over- or undersubtracting the AGN emission can bias the centroid position. Furthermore, the choice of smoothing technique can also lead to shifts in the derived X-ray centroid. Deeper X-ray imaging of all of the systems would help to address these centroiding issues.

Another complexity that enters into the determination of the BGG–X-ray offsets is the difficulty for some of the systems in identifying the BGG. For many of the groups there is no clearly dominant central galaxy. Instead, in several of the groups (B0712, B1608-3, B2108, and possibly PG 1115) the brightest and next brightest galaxies are separated by less than half a magnitude. Other investigations of intermediate-redshift groups (Mulchaey et al. 2006; Jeltema et al. 2006) have found systems for which the

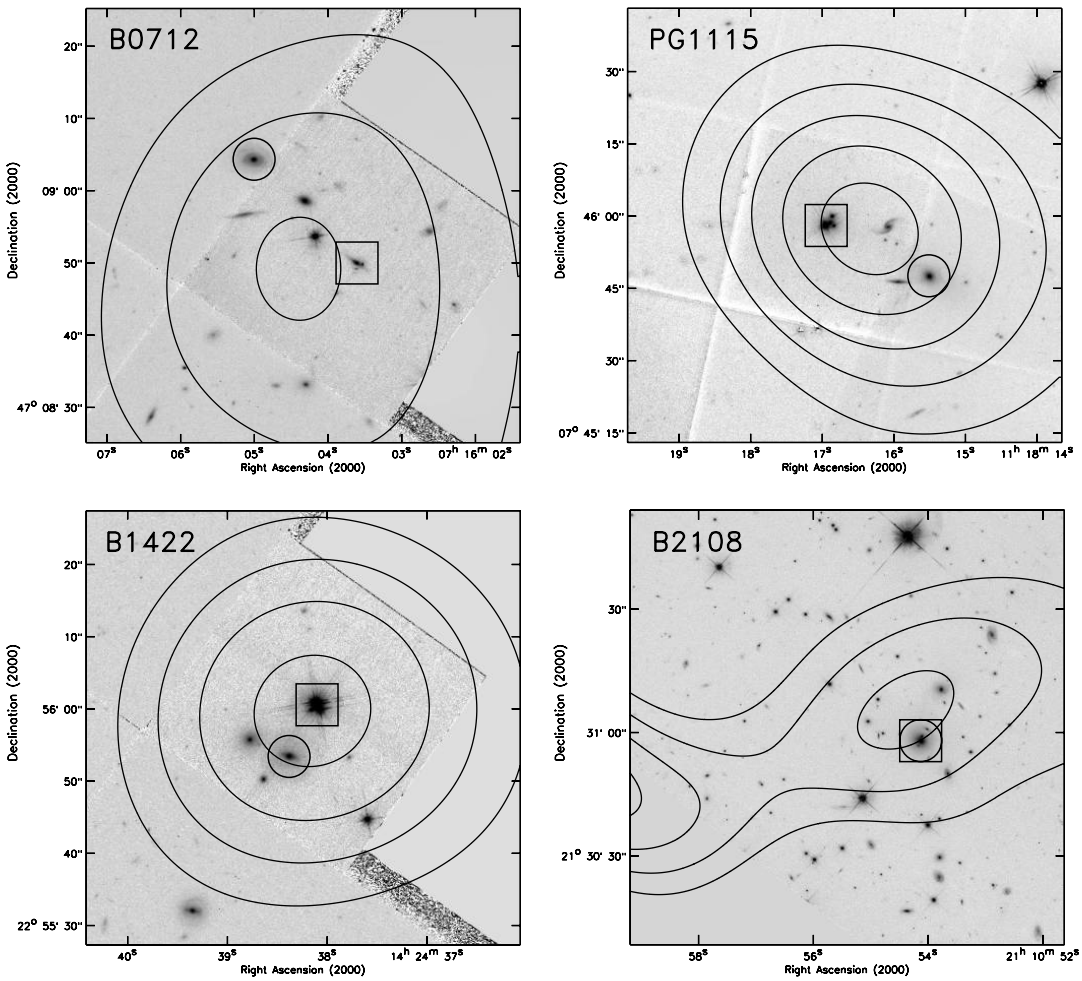

Fig. 9.—Optical imaging from the *HST* of the X-ray–detected groups, with contours representing the diffuse X-ray emission overlaid. For the B0712, PG 1115, and B2108 images, the data were taken with the F814W filter. For the B1422 image, the data were taken with the F791W filter. In each image the BGG is marked with a circle, and the lens system is marked with a box. Note that the lens system in the B0712 group is not physically associated with the group.

TABLE 5
Group Early-Type Fractions

Lens System	$N_{\rm tot}$	N_{HST}	$N_{\rm E/S0}$	f_e
B0712	15	9	5	0.56
PG 1115	13	7	5	0.71
B1422	16	7	5	0.71
B1600	7	7	1	0.14
B1608-1	10	9	2	0.22
B1608-3	8	7	6	0.85
B2108	47	24	15	0.62

IGM is detected in X-rays, but no dominant BGG was identified. For our lens group sample, the lack of a dominant BGG in some groups may be due to seeing these groups at an earlier stage of their evolution (e.g., Jeltema et al. 2007), or it may just be due to incomplete spectral information where the BGG has not yet been identified as a group member. Deeper optical data are needed to resolve this issue.

5.6. *Implications for Gravitational Lensing*

When a gravitational lens system resides in an overdense environment, that environment can impact the lensing potential and have a clear effect on cosmological and astrophysics measurements made using the lens (e.g., Keeton & Zabludoff 2004). An advantage of X-ray observations over spectroscopic surveys of the lens environments is that, in theory, the X-ray data can produce clear determinations of the center of the group potential and the total group mass (through the temperature of the X-ray gas). However, the existing *Chandra* data presented here are not sensitive enough to make robust measurements of either the centroids or the temperatures of the X-ray gas distributions.

5.7. *Galaxy Properties*

In low-redshift groups, correlations have been found between the morphological distribution of the member galaxies and the overall group properties (e.g., Zabludoff & Mulchaey 1998; Mulchaey & Zabludoff 1998; Osmond & Ponman 2004). In particular, the fraction of early-type galaxies shows a significant correlation with such properties as the group velocity dispersion and whether the group has detectable diffuse X-ray emission. At the redshifts of the lens-selected sample, it is not possible to use ground-based imaging to robustly determine galaxy morphologies. Therefore, we have used *HST* imaging to determine morphological properties of the group members whenever possible. For nearly all of the systems, we used archival WFPC2 or ACS imaging (GO-5699, PI: Impey; GO-5908, PI: Jackson; GO-6555, PI: Schechter; GO-6652, PI: Impey; GO-7495, PI: Falco; GO-8628, PI: Impey; GO-9133, PI: Falco; GO-9138, PI: Impey; GO-9744, PI: Kochanek). Most of these archival data sets were obtained by the CfA-Arizona Space Telescope Lens Survey team. For B1608 we used our own deep ACS imaging (GO-10158: PI: Fassnacht). Table 5 lists the proportion of galaxies identified by morphology as early-type (E or S0) in the lens-selected groups. All of the groups for which diffuse X-ray emission has been detected have relatively high early-type fractions, ranging from $\sim$50% to 70%. For galaxy groups in the local universe, the groups for which a diffuse intragroup X-ray component is detected also have significant early-type fractions. In contrast, the group associated with B1600, which has no detected X-ray emission, has only one early-type galaxy among its confirmed members. The B1608 groups are mixed, with B1608-1 having a low early-type fraction and B1608-3 having a high fraction. It may be that diffuse X-ray emission was not detected in the B1608-3 group simply because the group is at a high redshift and the observations were not particularly deep. It should be noted that the results in Table 5 must be considered with caution. First, the number of member galaxies that have high-resolution imaging is small because the fields of view of the *HST* cameras are limited. Second,the fractions may well be biased because the small fields are centered on the lens galaxy and may be probing special regions of the groups, such as the group centers.

5.8. *The Nature of the Lens-selected Groups*

Although the lens-selected group sample is small, the trends from the sample are suggestive. As discussed in the previous sections, the systems for which diffuse X-ray emission has been detected appear to be quite similar to local X-ray–loud samples in their luminosities, their locations on the $L_{\rm X}$-σ plot, and their early-type fractions. This may not be totally unexpected, as the lensing galaxies in strong lens systems tend to have early-type morphologies, and local groups containing massive ellipticals are more likely to have detectable X-ray emission (e.g., Mulchaey et al. 1996; Mulchaey & Zabludoff 1998). In fact, the one group in the lens-selected sample in which the lensing galaxy is clearly a spiral also has the lowest early-type fraction and is one of the X-ray nondetections. Thus, while the B1600 group and possibly the B1608-1 group appear to be like the typical group found in the local universe, with low masses and low early-type fractions (e.g., Geller & Huchra 1983; Eke et al. 2004), the majority of the lens group sample is more similar to the local groups for which X-ray emission from the IGM has been detected, which are more massive and dominated by early-type galaxies. The one lens group that does not fit this picture is the B1608-3 group, with its high early-type fraction and a relatively high velocity dispersion. The nondetection of B1608-3 in the *Chandra* observations may be due to a combination of its redshift and the short exposure time used in the observations. We feel that this is the group most likely to be detected if deeper observations of the field are undertaken.

6. SUMMARY AND FUTURE WORK

In this paper we have presented the results of a systematic analysis of ground-based optical spectroscopy and *Chandra* observations of fields containing both strong gravitational lenses and previously known moderate-redshift galaxy groups. Diffuse emission from four of the seven groups was detected in the X-ray observations, and the properties of these four groups were found to be similar to low-redshift X-ray–detected groups. For these four lens systems, we have found associated groups that appear to be gravitationally bound structures, based on both the detection of diffuse X-ray emission from the IGM and the redshift distribution of the group members. Although these are small-number statistics, it appears that galaxy groups selected by their association with gravitational lenses are massive and X-ray luminous. Therefore, it may be possible to find massive groups at moderate redshifts by conducting targeted and sensitive X-ray observations of lens systems.

We note that most of the lens-selected groups were detected only at low significance, and thus a full analysis of their X-ray properties was not possible. For example, precise X-ray temperatures could not be determined for any of the groups, and the determinations of the group centroids also remain highly uncertain. Therefore, deeper X-ray observations of the sample, in particular of the B1600 and B1608 fields, are important to clarify the conclusions that can be drawn from this nontraditional sample of moderate-redshift groups. Similarly, more extensive optical spectroscopy of the lens fields would allow better determinations of group memberships,

velocity dispersions, and the identities of the BGGs. Furthermore, additional lens group associations have been identified spectroscopically and are at redshifts that can be probed by deep *Chandra* observations. Having a larger sample is key to quantifying the properties of lens-selected galaxy groups.

We thank the anonymous referee for suggestions that improved the paper. Support for this work was provided by the National Aeronautics and Space Administration through *Chandra* Awards GO3-4167X and GO6-7125X issued by the *Chandra* X-Ray Observatory Center, which is operated by the Smithsonian Astrophysical Observatory for and on behalf of the National Aeronautics Space Administration under contract NAS8-03060. This work is based in part on observations made with the National Aeronautics and Space Administration (NASA)/ESA *Hubble Space Telescope*, obtained from the Data Archive at the Space Telescope Science Institute (STScI). STScI is operated by the Association of Universities for Research in Astronomy, Inc., under NASA contract NAS5-26555. These observations are associated with program AR-10300, supported by NASA through a grant from STScI. This work is supported in part by the European Community's Sixth Framework Marie Curie Research Training Network Programme, contract MRTN-CT-2004-505183 "ANGLES." Some of the data presented herein were obtained at the W. M. Keck Observatory, which is operated as a scientific partnership among the California Institute of Technology, the University of California, and the National Aeronautics and Space Administration. The Observatory was made possible by the generous financial support of the W. M. Keck Foundation. The authors wish to recognize and acknowledge the very significant cultural role and reverence that the summit of Mauna Kea has always had within the indigenous Hawaiian community. We are most fortunate to have the opportunity to conduct observations from this mountain. We are thankful for the dedication and expertise of the staffs of *Chandra*, *HST*, and the Keck observatories, without whom these observations would not have been possible.

Facilities: CXO, HST (ACS, WFPC2), Keck:I (LRIS)

APPENDIX A

SERENDIPITOUS SOURCES

In addition to studying the B0712 and B2108 groups, we also searched for diffuse and pointlike serendipitous sources in the fields of each system. Object detection was carried out with the CIAO tool `wavdetect` (Freeman et al. 2002), which was run with a detection threshold of 10^{-6} on the ACIS chips 2, 3, 5, 6, and 7. We used scales following the standard $(\sqrt{2})^i$ series with a maximum wavelet radius of 32 pixels. Sources were detected in both the soft (0.5–2.0 keV) and hard (2.0–8.0 keV) bands separately and cross-correlated; those detected with a 3 σ significance or greater in at least one band were included in the final source list. Photometry was carried out in the soft, hard, and full (0.5–8.0 keV) bands for pointlike objects on the unfiltered event files using the ACIS Extract package. Two diffuse sources were detected, one on chip 3 (ACIS-I3) of the B0712 data set and one on chip 7 (ACIS-S3) of the B2108 data set; photometry of these sources was carried out manually using the `dmextract` task. The final source lists, including both pointlike and diffuse objects, along with the counts detected in all three bands and the significances with which the sources were detected, are listed in Tables 6 and 7. The significances are calculated as the net counts from each source divided by the error of the background counts in the measurement aperture, $\sigma = \mathrm{NETCOUNTS}/(1 + \sqrt{\mathrm{BKGCOUNTS} + 0.75})$.

TABLE 6
SERENDIPITOUS SOURCES DETECTED IN THE FIELD OF B0712+472

NAME	R.A. (deg)	DECL. (deg)	NET COUNTS[a]			SIGNIFICANCE[a]		
			Soft	Hard	Full	Soft	Hard	Full
CXO J071654.3+471116[b]	109.22606	47.18790	1097	95	1192	37.6	2.0	21.3
CXO J071628.8+472120	109.12033	47.35569	37	24	61	4.7	2.8	5.5
CXO J071644.9+471858	109.18733	47.31631	15	26	41	2.6	3.3	4.4
CXO J071629.6+471506	109.12341	47.25172	75	44	119	7.7	5.6	9.8
CXO J071628.5+471725	109.11887	47.29028	25	30	55	3.7	3.8	5.6
CXO J071643.4+472123	109.18121	47.35664	38	18	56	4.7	2.5	5.4
CXO J071729.4+471445	109.37275	47.24597	64	43	106	6.2	4.3	7.7
CXO J071713.6+471150	109.30704	47.19747	29	25	54	4.1	2.9	5.0
CXO J071709.5+471259	109.28987	47.21639	134	56	190	10.2	5.4	11.6
CXO J071641.8+471516	109.17429	47.25447	19	24	43	3.2	3.5	5.0
CXO J071517.9+471713	108.82471	47.28706	109	29	138	8.9	2.5	8.4
CXO J071516.4+472102	108.81854	47.35075	49	1	50	4.9	0.1	3.6
CXO J071515.9+471614	108.81650	47.27078	21	20	41	3.3	2.4	4.1
CXO J071510.9+471549	108.79575	47.26372	54	13	67	5.6	1.2	4.7
CXO J071500.8+471819	108.75371	47.30533	34	0	31	3.8	0.0	2.3
CXO J071459.0+472048	108.74605	47.34692	51	0	29	4.9	0.0	2.0
CXO J071448.2+472044	108.70087	47.34566	32	0	26	3.6	0.0	2.0
CXO J071442.8+472204	108.67871	47.36786	40	17	57	3.9	1.6	4.0
CXO J071457.6+471628	108.74025	47.27464	26	26	52	3.2	2.1	3.6
CXO J071545.1+471836	108.93796	47.31000	53	35	87	6.0	4.0	7.4
CXO J071540.9+470852	108.92054	47.14789	122	210	332	10.1	13.5	17.2
CXO J071558.5+471517	108.99392	47.25486	37	16	53	5.2	3.0	6.2
CXO J071549.6+471143	108.95696	47.19545	18	16	34	3.4	3.1	4.9
CXO J071559.9+471224	108.99966	47.20678	29	17	45	4.4	3.2	5.8

TABLE 6—*Continued*

Name	R.A. (deg)	Decl. (deg)	Net Counts[a]			Significance[a]		
			Soft	Hard	Full	Soft	Hard	Full
CXO J071546.8+471404	108.94525	47.23461	70	44	113	7.4	5.6	9.6
CXO J071533.7+471038	108.89050	47.17739	24	10	33	3.9	2.2	4.8
CXO J071528.9+471729	108.87075	47.29144	45	0	41	5.4	0.0	4.3
CXO J071525.1+471059	108.85475	47.18330	32	0	32	4.7	0.1	4.7
CXO J071524.9+471104	108.85379	47.18467	37	2	39	5.1	0.7	5.2
CXO J071516.3+471604	108.81796	47.26778	30	19	48	4.2	2.7	5.1
CXO J071511.8+471451	108.79933	47.24767	26	9	35	3.7	1.4	3.9
CXO J071550.1+471424	108.95908	47.24011	15	0	15	3.0	0.0	2.9
CXO J071548.0+471709	108.95016	47.28608	19	1	19	3.3	0.2	3.1
CXO J071545.8+471340	108.94100	47.22786	23	10	32	3.8	2.2	4.7
CXO J071542.2+471333	108.92592	47.22603	1	18	19	0.5	3.2	3.3
CXO J071532.8+470926	108.88704	47.15722	3	16	19	0.9	3.1	3.4
CXO J071521.9+471141	108.84158	47.19483	0	22	22	0.0	3.8	3.8
CXO J071522.1+471136	108.84217	47.19333	3	42	44	0.9	5.5	5.7
CXO J071607.9+471428	109.03320	47.24111	7	16	22	1.7	3.0	3.7
CXO J071610.7+470515	109.04496	47.08764	96	22	119	8.8	3.8	9.9
CXO J071611.0+470856	109.04601	47.14903	26	8	33	4.2	1.9	4.8
CXO J071620.3+471119	109.08471	47.18878	10	25	35	2.3	4.1	4.9
CXO J071607.8+470613	109.03267	47.10375	23	20	43	3.8	3.5	5.5
CXO J071627.6+470639	109.11521	47.11089	348	66	415	17.7	7.1	19.3
CXO J071628.5+470508	109.11913	47.08558	21	37	58	3.6	4.9	6.4
CXO J071636.6+470917	109.15279	47.15475	29	9	38	4.4	2.0	5.0
CXO J071630.4+470525	109.12688	47.09031	25	0	24	4.0	0.0	3.7
CXO J071625.9+470751	109.10829	47.13094	84	7	92	8.2	1.8	8.6
CXO J071615.4+470323	109.06421	47.05661	54	14	68	6.3	2.5	7.0
CXO J071610.6+471241	109.04441	47.21144	147	0	147	11.1	0.2	11.1
CXO J071604.2+470751	109.01784	47.13097	22	5	26	3.8	1.3	4.2

[a] Soft, 0.5–2.0 keV; hard, 2.0–8.0 keV; full, 0.5–8.0 keV.
[b] Extended source.

TABLE 7

SERENDIPITOUS SOURCES DETECTED IN THE FIELD OF B2108+213

NAME	R.A. (deg)	DECL. (deg)	NET COUNTS[a]			SIGNIFICANCE[a]		
			Soft	Hard	Full	Soft	Hard	Full
CXO J211043.4+213404[b]	317.68085	21.56785	330	153	483	17.6	6.0	13.5
CXO J211034.4+213837	317.64349	21.64375	13	23	36	2.6	3.4	4.5
CXO J211022.2+214207	317.59253	21.70203	27	0	23	3.8	0.0	2.6
CXO J211018.4+213708	317.57684	21.61889	18	11	28	3.1	2.0	3.9
CXO J211007.6+214323	317.53174	21.72319	43	19	62	4.7	2.3	5.3
CXO J211004.8+214358	317.52005	21.73281	23	0	17	3.1	0.0	1.7
CXO J211116.8+213951	317.82001	21.66442	19	21	40	3.0	2.9	4.4
CXO J211111.1+214013	317.79663	21.67033	74	54	128	7.4	5.9	9.7
CXO J211055.3+214037	317.73053	21.67711	102	12	114	9.0	1.8	9.0
CXO J211053.2+213831	317.72202	21.64206	19	11	29	3.3	2.2	4.2
CXO J211048.7+214246	317.70322	21.71297	36	22	58	4.5	2.8	5.4
CXO J211004.7+212510	317.51959	21.41945	222	17	238	13.3	1.6	12.5
CXO J211003.5+212622	317.51474	21.43947	47	14	61	5.1	1.4	4.6
CXO J211001.7+213149	317.50708	21.53047	105	5	109	8.4	0.5	7.0
CXO J210959.5+212826	317.49814	21.47389	42	20	62	4.7	1.9	4.7
CXO J210956.8+213023	317.48691	21.50642	34	0	30	3.9	0.0	2.4
CXO J211034.2+213312	317.64288	21.55358	45	22	67	5.8	3.8	7.2
CXO J211023.6+213310	317.59839	21.55289	4	22	27	1.3	3.7	4.1
CXO J211020.8+213255	317.58698	21.54883	24	18	42	3.9	3.2	5.4
CXO J211018.6+212955	317.57776	21.49875	24	1	25	3.9	0.4	3.9
CXO J211013.0+212549	317.55420	21.43031	87	34	121	8.0	4.2	9.3
CXO J211116.4+213250	317.81842	21.54736	374	207	581	18.3	13.3	23.0
CXO J211114.2+213554	317.80923	21.59853	71	28	99	7.4	4.2	8.8
CXO J211113.1+213443	317.80475	21.57875	16	5	21	3.0	1.1	3.3
CXO J211108.6+213052	317.78604	21.51455	18	1	19	3.4	0.3	3.4
CXO J211105.4+212950	317.77249	21.49747	22	10	32	3.7	2.3	4.7
CXO J211104.2+212747	317.76785	21.46331	3	28	31	1.0	4.3	4.6
CXO J211102.0+213444	317.75867	21.57889	17	4	22	3.3	1.2	3.7
CXO J211056.7+213315	317.73660	21.55422	38	20	57	5.2	3.5	6.6
CXO J211055.6+212732	317.73199	21.45903	20	4	24	3.5	1.2	3.9
CXO J211052.6+213239	317.71918	21.54431	23	23	45	3.9	3.9	5.8
CXO J211051.3+213459	317.71381	21.58311	16	16	32	3.1	3.1	4.6
CXO J211050.1+213247	317.70898	21.54642	24	5	28	4.0	1.4	4.4
CXO J211047.3+212804	317.69742	21.46795	70	1	70	7.4	0.2	7.4

[a] Soft, 0.5–2.0 keV; hard, 2.0–8.0 keV; full, 0.5–8.0 keV.

[b] Extended source.

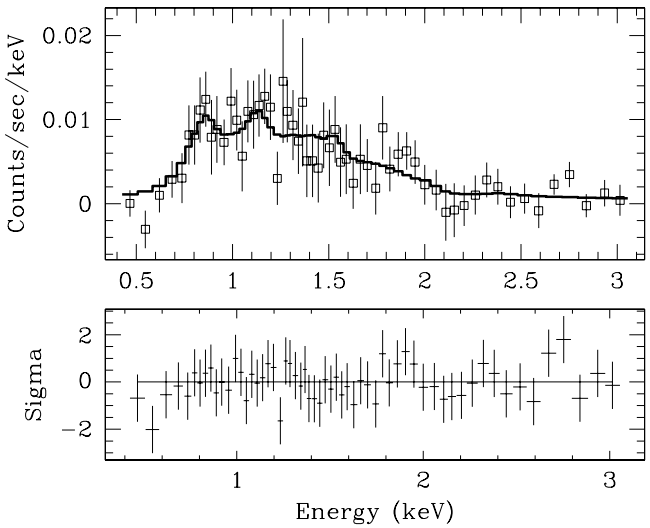

FIG. 10.— Spectral fit to the observed energy spectrum of ZwCl 0713.1+4717. The spectrum has been background subtracted and grouped to contain at least 30 counts per bin. The best-fit Raymond-Smith thermal spectrum has a temperature of 1.78 keV and a redshift of 0.30.

We searched for known counterparts to the two detected diffuse sources and found one to be 1.1′ from the reported position of the Zwicky cluster Zwcl 0713.1+4717 (Zwicky et al. 1966). We extracted the spectrum of the cluster using the `specextract` task and fit to it an absorbed Raymond-Smith thermal plasma model with a 0.3 solar metal abundance. Allowing both the temperature and the redshift to vary, our best-fit model returned a temperature of 1.78 keV and a redshift of 0.30. The extracted spectrum and our best-fit thermal model are shown in Figure 10. We found no such counterpart to the diffuse source detected in the field of B2108. Furthermore, an extraction of its spectrum proved inconclusive, as we could not fit to it a thermal or power law model.

REFERENCES

Aarseth, S. J., & Fall, S. M. 1980, ApJ, 236, 43
Auger, M. W., Fassnacht, C. D., Abrahamse, A. L., Lubin, L. M., & Squires, G. K. 2007, AJ, 134, 668
Auger, M. W., Fassnacht, C. D., Wong, K. C., Thompson, D., Matthews, K., & Soifer, B. T. 2008, ApJ, 673, 778
Balogh, M. L., et al. 2007, MNRAS, 374, 1169
Barkana, R. 1997, ApJ, 489, 21
Barnes, J. 1985, MNRAS, 215, 517
Beers, T. C., Flynn, K., & Gebhardt, K. 1990, AJ, 100, 32
Browne, I. W. A., Patnaik, A. R., Wilkinson, P. N., & Wrobel, J. M. 1998, MNRAS, 293, 257
Browne, I. W. A., et al. 2003, MNRAS, 341, 13
Burud, I., et al. 2000, ApJ, 544, 117
Carlberg, R. G., Yee, H. K. C., Morris, S. L., Lin, H., Hall, P. B., Patton, D. R., Sawicki, M., & Shepherd, C. W. 2001, ApJ, 552, 427
Dai, X., & Kochanek, C. S. 2005, ApJ, 625, 633
Davis, M., et al. 2003, Proc. SPIE, 4834, 161
Dickey, J. M., & Lockman, F. J. 1990, ARA&A, 28, 215
Dressler, A. 1980, ApJ, 236, 351
Ebeling, H., White, D. A., & Rangarajan, F. V. N. 2006, MNRAS, 368, 65
Eke, V. R., et al. 2004, MNRAS, 348, 866
Fang, T., et al. 2007, ApJ, 660, L27
Fassnacht, C. D., & Cohen, J. G. 1998, AJ, 115, 377
Fassnacht, C. D., Gal, R. R., Lubin, L. M., McKean, J. P., Squires, G. K., & Readhead, A. C. S. 2006a, ApJ, 642, 30
Fassnacht, C. D., & Lubin, L. M. 2002, AJ, 123, 627
Fassnacht, C. D., Pearson, T. J., Readhead, A. C. S., Browne, I. W. A., Koopmans, L. V. E., Myers, S. T., & Wilkinson, P. N. 1999, ApJ, 527, 498
Fassnacht, C. D., Womble, D. S., Neugebauer, G., Browne, I. W. A., Readhead, A. C. S., Matthews, K., & Pearson, T. J. 1996, ApJ, 460, L103
Fassnacht, C. D., Xanthopoulos, E., Koopmans, L. V. E., & Rusin, D. 2002, ApJ, 581, 823
Fassnacht, C. D., et al. 2006b, ApJ, 651, 667
Freeman, P. E., Kashyap, V., Rosner, R., & Lamb, D. Q. 2002, ApJS, 138, 185
Gal, R. R., Lemaux, B. C., Lubin, L. M., Kocevski, D., & Squires, G. K. 2007, ApJ, submitted (arXiv:0803.3842)
Garmire, G. P., Bautz, M. W., Ford, P. G., Nousek, J. A., & Ricker, G. R., Jr. 2003, Proc. SPIE, 4851, 28
Gastaldello, F., Trevese, D., Vagnetti, F., & Fusco-Femiano, R. 2008, ApJ, 673, 176
Geller, M. J., & Huchra, J. P. 1983, ApJS, 52, 61
Gerke, B. F., et al. 2005, ApJ, 625, 6
Grant, C. E., Bautz, M. W., Chartas, G., & Garmire, G. P. 2004, ApJ, 610, 686
Hammer, F., Rigaut, F., Angonin-Willaime, M.-C., & Vanderriest, C. 1995, A&A, 298, 737
Helsdon, S. F., & Ponman, T. J. 2000, MNRAS, 315, 356
Helsdon, S. F., Ponman, T. J., & Mulchaey, J. S. 2005, ApJ, 618, 679
Henry, J. P., & Heasley, J. N. 1986, Nature, 321, 139
Hogg, D. W., & Blandford, R. D. 1994, MNRAS, 268, 889
Holder, G. P., & Schechter, P. L. 2003, ApJ, 589, 688
Horner, D. 2001, Ph.D. thesis, Univ. Maryland
Impey, C. D., Falco, E. E., Kochanek, C. S., Lehár, J., McLeod, B. A., Rix, H.-W., Peng, C. Y., & Keeton, C. R. 1998, ApJ, 509, 551
Jackson, N., et al. 1995, MNRAS, 274, L25
———. 1998, MNRAS, 296, 483
Jeltema, T. E., Mulchaey, J. S., Lubin, L. M., & Fassnacht, C. D. 2007, ApJ, 658, 865
Jeltema, T. E., Mulchaey, J. S., Lubin, L. M., Rosati, P., & Böhringer, H. 2006, ApJ, 649, 649
Keeton, C. R., Christlein, D., & Zabludoff, A. I. 2000, ApJ, 545, 129
Keeton, C. R., & Zabludoff, A. I. 2004, ApJ, 612, 660
Koopmans, L. V. E., de Bruyn, A. G., Xanthopoulos, E., & Fassnacht, C. D. 2000, A&A, 356, 391
Kundić, T., Cohen, J. G., Blandford, R. D., & Lubin, L. M. 1997a, AJ, 114, 507
Kundić, T., Hogg, D. W., Blandford, R. D., Cohen, J. G., Lubin, L. M., & Larkin, J. E. 1997b, AJ, 114, 2276
Mahdavi, A., Böhringer, H., Geller, M. J., & Ramella, M. 2000, ApJ, 534, 114
Markevitch, M. 1998, ApJ, 504, 27
McKean, J. P., et al. 2005, MNRAS, 356, 1009
Merritt, D. 1985, ApJ, 289, 18
Momcheva, I., Williams, K., Keeton, C., & Zabludoff, A. 2006, ApJ, 641, 169
More, A., McKean, J. P., Muxlow, T. W. B., Porcas, R. W., Fassnacht, C. D., & Koopmans, L. V. E. 2008, MNRAS, 384, 1701
Mulchaey, J. S. 2000, ARA&A, 38, 289
Mulchaey, J. S., Davis, D. S., Mushotzky, R. F., & Burstein, D. 1996, ApJ, 456, 80
Mulchaey, J. S., Lubin, L. M., Fassnacht, C., Rosati, P., & Jeltema, T. E. 2006, ApJ, 646, 133
Mulchaey, J. S., & Zabludoff, A. I. 1998, ApJ, 496, 73
Myers, S. T., et al. 1995, ApJ, 447, L5
———. 2003, MNRAS, 341, 1
Oguri, M. 2005, MNRAS, 361, L38
Oguri, M., Keeton, C. R., & Dalal, N. 2005, MNRAS, 364, 1451

Oke, J. B., et al. 1995, PASP, 107, 375
Osmond, J. P. F., & Ponman, T. J. 2004, MNRAS, 350, 1511
Patnaik, A. R., Browne, I. W. A., Walsh, D., Chaffee, F. H., & Foltz, C. B. 1992a, MNRAS, 259, 1P
Patnaik, A. R., Browne, I. W. A., Wilkinson, P. N., & Wrobel, J. M. 1992b, MNRAS, 254, 655
Patnaik, A. R., Kemball, A. J., Porcas, R. W., & Garrett, M. A. 1999, MNRAS, 307, L1
Pooley, D., Blackburne, J. A., Rappaport, S., Schechter, P. L., & Fong, W.-F. 2006, ApJ, 648, 67
Rasmussen, J., Ponman, T. J., Mulchaey, J. S., Miles, T. A., & Raychaudhury, S. 2006, MNRAS, 373, 653
Rykoff, E. S., et al. 2008, ApJ, 675, 1106
Schechter, P. L., et al. 1997, ApJ, 475, L85
Tonry, J. L. 1998, AJ, 115, 1
Turner, E. L., & Gott, J. R., III. 1976, ApJS, 32, 409
Voges, W., et al. 1999, A&A, 349, 389
Weymann, R. J., et al. 1980, Nature, 285, 641
Wilkinson, P. N., Browne, I. W. A., Patnaik, A. R., Wrobel, J. M., & Soratia, B. 1998, MNRAS, 300, 790
Williams, K. A., Momcheva, I., Keeton, C. R., Zabludoff, A. I., & Lehár, J. 2006, ApJ, 646, 85
Willis, J. P., et al. 2005a, MNRAS, 363, 675
———. 2005b, MNRAS, 364, 751
Wilman, D. J., Balogh, M. L., Bower, R. G., Mulchaey, J. S., Oemler, A., Jr., Carlberg, R. G., Morris, S. L., & Whitaker, R. J. 2005, MNRAS, 358, 71
Yee, H. K. C., et al. 2000, ApJS, 129, 475
York, D. G., et al. 2000, AJ, 120, 1579
Young, P., Deverill, R. S., Gunn, J. E., Westphal, J. A., & Kristian, J. 1981, ApJ, 244, 723
Zabludoff, A. I., & Mulchaey, J. S. 1998, ApJ, 496, 39
Zwicky, F., Herzog, E., & Wild, P. 1966, Catalogue of Galaxies and of Clusters of Galaxies (Pasadena: California Institute of Technology)